




Article

Construction of Laminated Luminescent Solar Concentrator “Smart” Window Based on Thermoresponsive Polymer and Carbon Quantum Dots

Bing Xu ^{1,*}, Jianying Wang ^{1,*}, Chen Cai ¹, Wei Xin ¹, Lai Wei ^{2,*}, Qinsi Yang ³, Bo Peng ³, Yuandu Hu ⁴ ,
Jinhua Li ^{1,*}  and Xianbao Wang ¹ 

¹ Key Laboratory for the Green Preparation and Application of Functional Materials, Hubei Key Laboratory of Polymer Materials, Collaborative Innovation Center for Advanced Organic Chemical Materials Co-Constructed by the Province and Ministry, School of Materials Science and Engineering, Hubei University, Ministry of Education, Wuhan 430062, China

² Wuhan Drug Solubilization and Delivery Technology Research Center, School of Life and Health, Wuhan Vocational College of Software and Engineering, Wuhan 430205, China

³ Wenzhou Institute, University of Chinese Academy of Sciences, Wenzhou 325000, China

⁴ Department of Materials Science and Engineering, School of Physical Sciences and Engineering, Beijing Jiaotong University, Beijing 100044, China

* Correspondence: wangjy_2002@163.com (J.W.); future361@163.com (L.W.); jinhua_li@hubu.edu.cn (J.L.)

Abstract: Conventional luminescent solar concentrators (LSCs) lack the ability of dynamic modulation, energy saving, and privacy protection. In this work, a thermoresponsive laminated LSC was created and further used as a “smart” window (SW). The laminated LSC “smart” window (LSC-SW) was prepared by introducing carbon quantum dots (CQDs) into the sandwiched LSCs filled with aqueous thermosensitive polymer (PNIPAm) solution. To realize better compatibility, two types of fluorescent materials, hydrophilic CQDs (blue and green emitting CQDs), had been synthesized. The LSC-SW showed a good dynamic response to the ambient temperature and solar irradiation, which can be switched between transparent (<32 °C) and opaque states (>32 °C). Besides, the optimal LSC-SW had high transmittance (>80%) at the transparent state and low transmittance (<10%) at the opaque state. More importantly, the opaque state enabled the LSC-SW with higher external optical efficiency (η_{opt} of 7.49%), energy saving.

Keywords: carbon dots; thermoresponsive polymer; luminescent solar concentrators; smart window; external optical efficiency



Citation: Xu, B.; Wang, J.; Cai, C.; Xin, W.; Wei, L.; Yang, Q.; Peng, B.; Hu, Y.; Li, J.; Wang, X. Construction of Laminated Luminescent Solar Concentrator “Smart” Window Based on Thermoresponsive Polymer and Carbon Quantum Dots. *Crystals* **2022**, *12*, 1612. <https://doi.org/10.3390/cryst12111612>

Academic Editors: Jing Wei and Fangze Liu

Received: 17 October 2022

Accepted: 8 November 2022

Published: 11 November 2022

Publisher’s Note: MDPI stays neutral with regard to jurisdictional claims in published maps and institutional affiliations.



Copyright: © 2022 by the authors. Licensee MDPI, Basel, Switzerland. This article is an open access article distributed under the terms and conditions of the Creative Commons Attribution (CC BY) license (<https://creativecommons.org/licenses/by/4.0/>).

1. Introduction

Building integrated photovoltaic (BIPV), that is, integrated PV into a part of buildings which can convert solar energy to electricity, has attracted increasing attention owing to partly supplying the electricity needs of buildings [1]. To date, commercial Si-based solar cells as one of the typical BIPVs have widely been used in the roof of buildings. To fully use the building area, recently, BIPV windows, integrating PV into the building’s window, have been developed which can provide a supplement source of electricity generation [2]. Compared to semitransparent Si-based or thin film solar cells, luminescent solar concentrators (LSCs) show great potential for the construction of BIPV windows owing to their advantages, such as low cost, high transparency, flexible architecture, ease of fabrication, good efficiency, and use of diffuse light [3,4]. LSCs are transparent optical devices which embedded fluorescent materials, e.g., dyes and quantum dots (QDs), into waveguide matrix (polymer substrate or polymer film coated on glass substrate) [5–8]. LSCs absorb sunlight and re-emit light of longer wavelengths via fluorescent materials. The part of re-emitted light can be waveguided to the edge of LSCs owing to total internal reflection, further harvested, and converted to electricity by the PV cell attached at the LSC edge. In the last

decade, various LSCs, including different fluorescent materials (e.g., perovskite QDs, AIE molecules, and carbon quantum dots (CQDs)), and varied architectures (e.g., single-layer, tandem, sandwiched structure), had been developed [9–23]. However, the majority of LSCs are static, the LSCs with dynamic modulation are highly desired, which can lead to smart BIPV windows.

Smart windows (SW) have good dynamic modulation ability, which not only changes the windows' colors, but tunes the windows' transparency once a stimulus is applied [24]. To date, various smart windows have been developed based on different tunable mechanisms, such as thermochromism [25–29], photochromism [30], mechanochromism [31], and electrochromism [32–38]. However, a majority of SWs focus on the tunability of color or transparency, and do not involve electricity generation. To realize smart BIPV windows, a combination of SWs and LSCs, e.g., an LSC smart window (LSC-SW), will be one of the effective strategies. In 2018, Debijs et al. reported a color-tunable LSC by introducing two kinds of liquid crystal (LC) molecules (coumarin derivative donor (Cou) and perylene diimide acceptor (PBI)) into the LC host (LC E7) [39]. The LSC could change the colors from green to red with the increase of ambient temperature from 40 to 70 °C based on the Förster resonance energy transfer (FRET) mechanism. Meanwhile, the colored LSC also gives good electricity generation, a total light power output of 25 mW (external optical efficiency $\eta_{\text{opt}} = 2.4\%$) in the cold state and 34 mW ($\eta_{\text{opt}} = 3.2\%$) in the warm state. Based on this, the same group created multistate LSC-SW by using supertwisted nematic (STN) LC cells, which can be switched between three states when controlling the applied voltage: one is the “dark” state for increased light absorption and electrical generation, second is the “light” state for transparency, and the third is the “scattering” state for enhanced haziness [40]. Importantly, the optimal η_{opt} of 3.8%, 3.0%, and 2.6% for dark, scattering, and light states, respectively, could be obtained. The multistate LSC-SW not only provided a good privacy feature but could be used as a diffuse glazing to increase plant growth in horticultural applications. Subsequently, Hong et al. developed another LSC-SW by using polymer-dispersed liquid crystals (PDLC) and CQDs [41]. The LSC-SW not only selectively harvested the ultraviolet light (UV) and near UV light for electrical energy generation without competing for the visible and near-infrared light, but could be switched between transparent and opaque states while simultaneously generating electrical energy. The best performance, η_{opt} of 4.52%, was obtained at the opaque state of LSC-SW. Although progress has been made, there are few reports of LSC-SWs and a majority of LSC-SWs have been constructed based on LC materials. Thus, it is a challenge to explore novel LSC-SW based on non-LC materials.

In this work, a thermoresponsive laminated LSC-SW was created by introducing CQDs into a laminated LSC filled with an aqueous thermosensitive polymer (PNIPAm) solution. The LSC-SW could be dynamically switched at transparent (<32 °C) and opaque (>32 °C) state under different ambient temperature, as shown in Figure 1. Correspondingly, high transmittance (>80%) in the transparent state and a low transmittance (<10%) in the opaque state was obtained and the power could be outputted from the PV cell on the edges [42]. More importantly, the opaque state of the LSC-SW not only led to higher external optical efficiency (η_{opt} of 7.49 %) but realized energy savings.

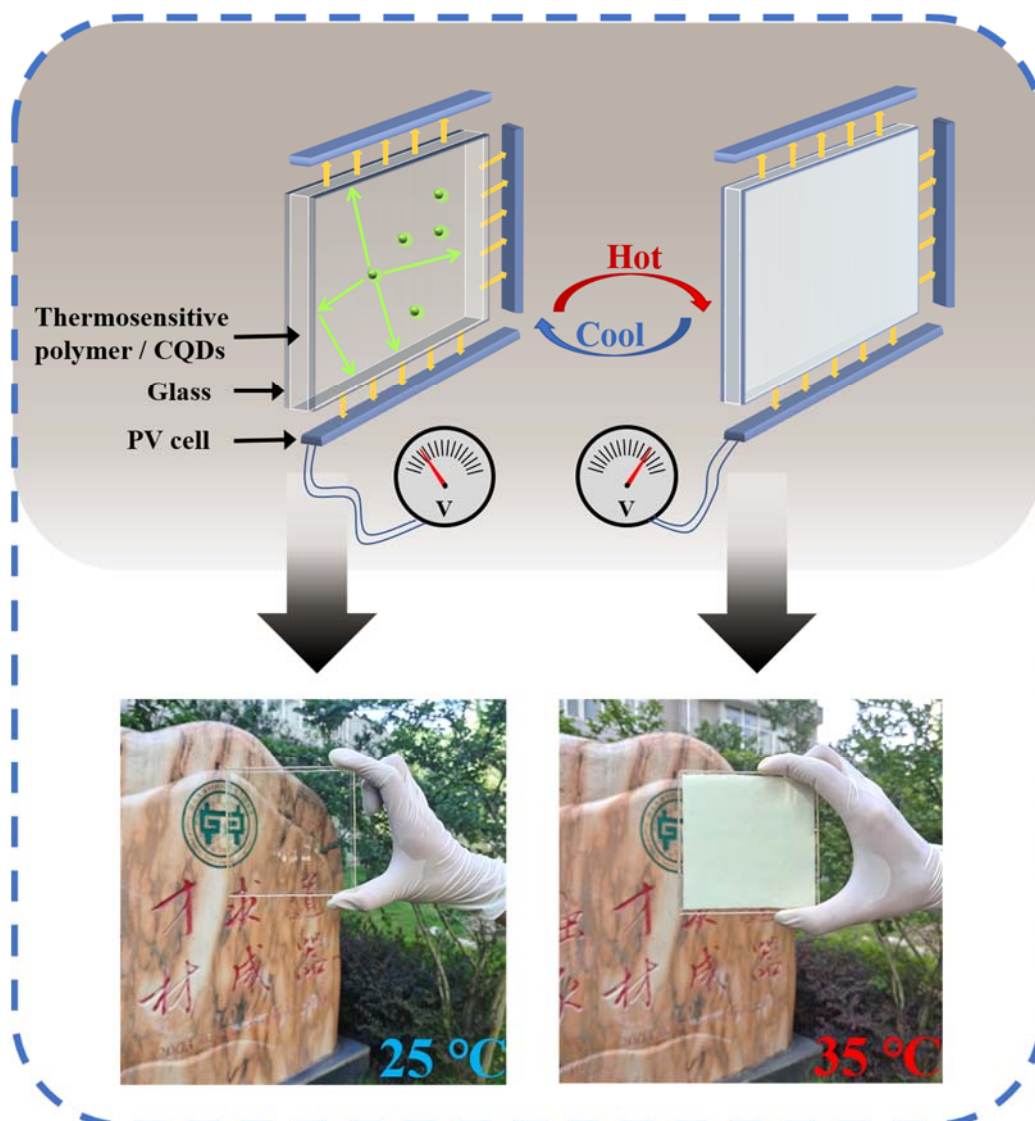


Figure 1. Schematic diagram and thermoresponse of LSC-SW by combining thermosensitive polymer and CQDs.

2. Experimental Section

2.1. Synthesis of Thermosensitive Polymer

Thermosensitive polymer (poly(*N*-isopropylacrylamide) (PNIPAm)) was synthesized by using the typical free radical polymerization [43]. Briefly, 1.29 g (0.011 mol) of NIPAm monomer was dissolved in 50 mL deionized water at 25 °C. After stirring, a transparent and clear homogeneous solution was obtained, which was transferred to the three-neck flask. Then, the above mixture was stirred and heated to 110 °C in an oil bath. After 10 min, 2 mL of aqueous solution containing 0.02 g KPS was added and further heated at 110 °C. After 60 min of polymerization, thermosensitive polymer PNIPAm was obtained, which was further purified by centrifugation and dialysis process.

2.2. Synthesis of CQDs

Blue-emitting CQDs (B-CQDs) and green-emitting CQDs (G-CQDs) were synthesized by the hydro/solvothermal method [17,44]. Briefly, the B-CQDs were synthesized from citric acid and Tris precursors. First, 3.5 g of citric acid and 2 g of Tris were dissolved in 20 mL of deionized water and fully stirred at room temperature for 10 min to form a transparent solution. Then, the solution was transferred to a 50 mL PTFE inner liner, which

was put into stainless steel autoclave. After that, the above mixture was heated at 200 °C for 10 h. After centrifugation at 10,000 r/min for 10 min and dialysis process, aqueous B-CQDs solution was obtained. The G-CQDs were synthesized from m-phenylenediamine (mPD). First, 30 mg of mPD was dissolved in 10 mL of ethanol and fully mixed for 10 min at room temperature to form a transparent solution. The following synthesis was the same as that of B-CQDs.

2.3. Fabrication of Laminated LSC-SW

Two kinds of high-transparent optical glass ($2.5 \times 2.5 \times 0.07 \text{ cm}^3$ and $2.5 \times 2.5 \times 0.03 \text{ cm}^3$) were used as the substrate. First, ethanol, acetone, deionized water, and ethanol were used for cleaning the glass substrate, respectively, followed by an ultrasonic process for 30 min. A laminated glass structure was prepared by using 3M tape strips with a thickness of 1 mm to separate the above two glasses at their edges, of which three edges were sealed by epoxy resin adhesive. A mixture of CQDs and PNIPAm was made by adding B-CQDs or G-CQDs into aqueous PNIPAm solutions. Then, the PNIPAm/CQDs mixture was injected into the laminated glass and sealed with epoxy resin adhesive. Finally, the laminated LSC-SW with various CQDs concentrations were obtained, which were further coupled with crystalline silicon solar cells for further testing. The detailed characterization of LSC-SW was summarized in the Supporting Information [45].

3. Results and Discussion

3.1. Synthesis and Properties of PNIPAm and CQDs

Thermosensitive polymer PNIPAm was first synthesized by free radical polymerization. The Fourier transform infrared (FTIR) and $^1\text{H-NMR}$ spectra had been used to confirm the PNIPAm structure. Figure 2a shows the FTIR spectrum of PNIPAm. It can be observed that the stretching vibration absorption peak of N–H of amide was at 3436 cm^{-1} , the stretching vibration absorption peak of C=O of amide was at 1651 cm^{-1} , and the bending vibration absorption peak of N-H of NIPAm was at 1543 cm^{-1} . It can be inferred that the obtained polymer contained an acrylamide structural unit. On the other hand, the stretching vibration absorption peaks at 2973 cm^{-1} and 2930 cm^{-1} were attributed to -CH_3 and -CH_2 , respectively. The absorption peaks at 1389 cm^{-1} and 1363 cm^{-1} corresponded to symmetric deformation vibration coupling splitting of isopropyl on the isopropyl group [46]. Figure 2b shows the $^1\text{H-NMR}$ spectrum of PNIPAm. The resonance peaks at 1.14 ppm and 4.01 ppm were attributed to methyl and methylene [$\text{-CH-(CH}_3)_2$] on isopropyl, respectively. In addition, the resonance peaks at 1.64 ppm and 2.10 ppm were attributed to methylene and methylene [$\text{-CH-CH}_2\text{-}$] on the main chain, respectively [47]. Thus, the above spectra data confirmed that the polymer PNIPAm had been successfully synthesized. PNIPAm is a typical thermosensitive polymer, which has a transition of low critical solution temperature (LCST, generally 32 °C) and changes the transparency at various temperatures. Figure 2c,d shows the optical photograph of aqueous PNIPAm solution at various temperatures. The aqueous PNIPAm solution showed a transparent state at low ambient temperature (25 °C) and an opaque state at high room temperature (35 °C), which further confirmed the obtainment of PNIPAm and their thermoresponsive properties.

Two kinds of hydrophilic CQDs, B-CQDs, and G-CQDs, were synthesized based on citric acid and aniline precursors, respectively. First, the morphology and size of B-CQDs and G-CQDs were confirmed by high-resolution transmission electron microscopy (HRTEM) measurements (Figure 3a,b). Figure 3a shows the B-CQDs had a spherical shape with a diameter of $\sim 3 \text{ nm}$. While the G-CQDs tended to aggregate during the preparation of the TEM sample. However, the crystalline CQDs also could be observed clearly (red circle), which appeared spherical shape with a diameter of $\sim 5 \text{ nm}$. Both B-CQDs and G-CQDs had a crystalline structure and the lattice fringe spacing was $\sim 0.21 \text{ nm}$, which is attributed to the $\langle 100 \rangle$ crystal plane in graphene [48]. On the other hand, the FTIR (Figure 3c,d) and X-ray photoelectron spectroscopy (XPS) spectra (Supplementary Materials Figure S1) had been con-

ducted to demonstrate the functional groups and chemical structure of the B-CQDs and G-CQDs. The FTIR spectra in Figure 3c,d show that the B-CQDs and G-CQDs surfaces had different functional groups, depending on their varied precursors. As for B-CQDs from citric acid and Tris, B-CQDs contained hydroxyl and carboxyl groups based on $\nu(\text{O}-\text{H})/\nu(\text{N}-\text{H})$ at 3430 cm^{-1} , $\nu(\text{C}=\text{O})$ at 1631 cm^{-1} , and $\nu(\text{C}-\text{O})$ at 1100 cm^{-1} . While G-CQDs had hydroxyl and amine groups, coming from $\nu(\text{O}-\text{H})/\nu(\text{N}-\text{H})$ at 3430 cm^{-1} , $\nu(\text{C}=\text{C})$ at 1560 cm^{-1} , and $\nu(\text{C}-\text{N})$ at 1345 cm^{-1} . The analysis of XPS spectra confirmed the existence of C, N, and O in the B-CQDs and G-CQDs (Supplementary Materials Figure S1a,d). For B-CQDs, the high-resolution XPS spectra of C 1s (Supplementary Materials Figure S1b) show that there were four C 1s in different chemical environments, corresponding to C=C at 284.43 eV, C-N at 285.25 eV, C-O at 286.67 eV, and C=O at 288.73 eV, respectively [49]. The high-resolution N 1s spectrum showed two different types of nitrogen doping: pyrrole nitrogen at 399.41 eV and graphite nitrogen at 400.34 eV (Supplementary Materials Figure S1c). While, the G-CQDs also showed a similar trend, which had three peaks at 284.91 eV, 399.21 eV, and 532.21 eV, corresponding to C 1s, N 1s, and O 1s, respectively (Supplementary Materials Figure S1d). In Supplementary Materials Figure S1e, four kinds of bonds, including C=C at 284.17 eV, C-N at 284.80 eV, C-O at 285.50 eV, and C-OH at 286.18 eV, are shown. Three different types of nitrogen doping: pyridine nitrogen, amino nitrogen, and pyrrole nitrogen at 398.39 eV, 399.16 eV, and 400.01 eV, respectively, existed in G-CQDs (Supplementary Materials Figure S1f). The above spectra further confirmed the CQDs surface contains rich functional groups, endowing the CQDs with good hydrophilic properties and compatibility with PNIPAm.

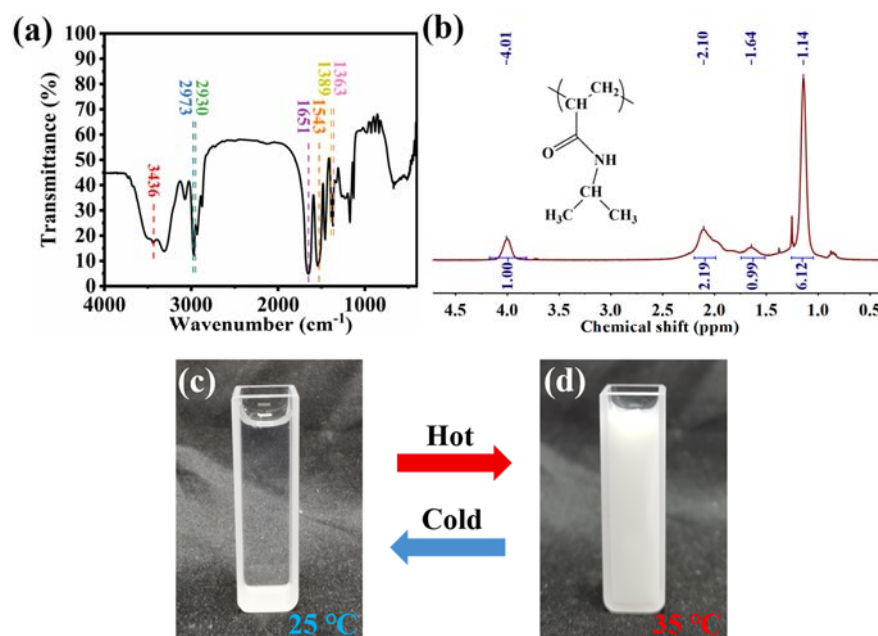


Figure 2. (a) FTIR spectrum of PNIPAm. (b) ^1H -NMR spectrum of PNIPAm. (c,d) The optical photograph of aqueous PNIPAm solution at 25 and 35 °C.

Subsequently, the optical properties of the B-CQDs and G-CQDs had been demonstrated. As shown in Figure 4a,d, both the B-CQDs and G-CQDs appeared one absorption peaks at ~ 360 and $\sim 380\text{ nm}$, respectively, which were attributed to the $n-\pi^*$ transitions of carboxyl, amine, or other aromatic structures in CQDs [17]. From the emission spectra, the emission peaks of the B-CQDs were located at 480 nm under 410 nm excitation, while the emission peaks of the G-CQDs were at 510 nm under 460 nm excitation, which well matched with the optical images of B-CQDs and G-CQDs under irradiation of UV light (the insets in Figure 4a,d). In addition, the B-CQDs and G-CQDs showed different excitation dependencies of PL emission spectra, as shown in Figure 4b,e. The B-CQDs showed the excitation dependence of PL emission, while the G-CQDs appeared the excitation indepen-

dence of PL emission, which comes from various surface states of CQDs, e.g., excitation independence induced by uniform surface state [17]. The PL decay curves of the B-CQDs and G-CQDs are shown in Figure 4c,f, and the average PL lifetimes were 15.1 ns and 9.8 ns, respectively. Correspondingly, the PLQYs of the B-CQDs and G-CQDs were 3.67% and 13.26%, respectively, as shown in Table S1.

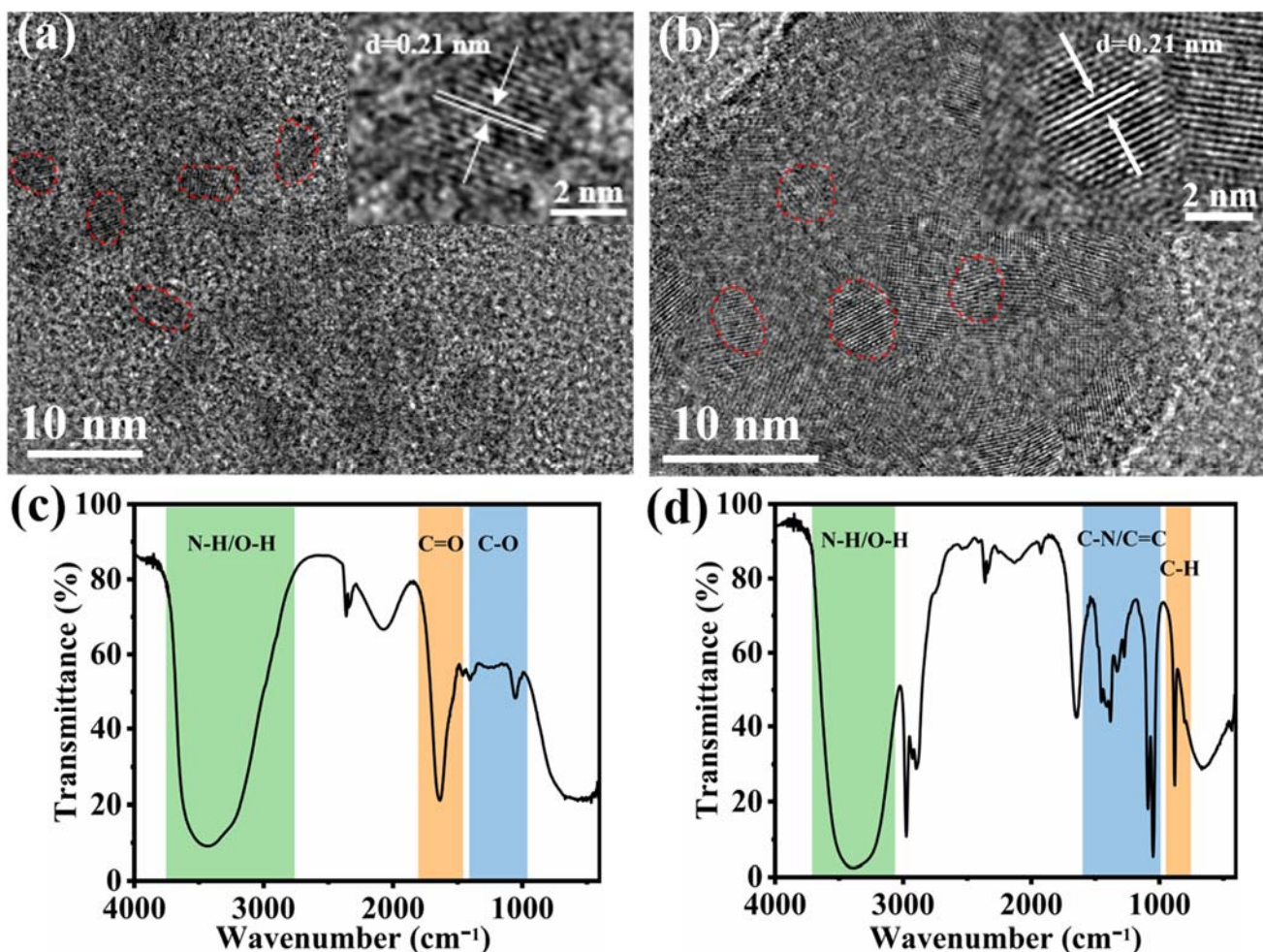


Figure 3. The HRTEM images of (a) B-CQDs and (b) G-CQDs. The FTIR spectra of (c) B-CQDs and (d) G-CQDs.

3.2. Fabrication and Performances of Laminated LSC-SW

The optical performance of B-CQDs and G-CQDs-based LSC-SWs (B-LSC-SW, G-LSC-SW) had first been demonstrated. Figure 5a shows the photograph of B-LSC-SW at 25 °C and 35 °C under natural light and 365 nm UV light, respectively. At low temperature (25 °C), the B-LSC-SW appeared highly transparent, and the words under the LSC-SW could be seen clearly; while, once the temperature was increased to 35 °C, the B-LSC-SW turned opaque, the words under LSC-SW could not be seen. Besides, whatever transparency or opaque state, the PL emission of B-LSC-SW was kept almost constant, emitting uniform blue color under irradiation of UV light. On the other hand, the G-LSC-SW give the same trend, e.g., becoming opaque at high temperature and emitting a uniform green color under UV light irradiation. Furthermore, to demonstrate the external optical efficiency (η_{opt}) of LSC-SWs, the typical *J-V* curves for LSCs with different CQDs concentrations had been measured (Figure 6a,c). The external optical efficiencies (η_{opt}) were plotted from the *J-V* curve data (Figure 6b,d). As for B-LSC-SW (Figure 6a,b), with the increase in B-CQDs concentrations in LSCs, the η_{opt} first enhanced and then reduced, e.g., at 25 °C, the η_{opt} changed the efficiencies from 2.13%, 2.45%, 2.61%, 2.45% to 2.53%, while, at 35 °C, the η_{opt}

was changed from 7.25%, 7.35%, 7.49%, 7.23%, to 7.04%. There is an optimal efficiency with the increased CQDs concentrations. The low performance at high CQDs concentrations was attributed to the aggregation-caused quenching (ACQ) effect of CQDs [50,51]. Importantly, the η_{opt} in the opaque state was 2–3 times higher than that in the transparent state, which probably resulted from the enhanced scattering effect induced by the opaque state at high temperature and the further enhanced waveguide effect of the LSCs [41]. On the other hand, the G-LSC-SW appeared the same trend, e.g., there was a maximum efficiency at optimal CQDs concentration. The maximum η_{opt} of 2.76% at 25 °C and 7.2% at 35 °C, respectively, had been achieved. The detailed photovoltaic parameters of the B- and G-LSC-SWs are listed in Tables S2 and S3, including values of V_{oc} , J_{sc} , FF , and η_{opt} . Since the waveguide materials are the same, the changing trend of η_{opt} with the CQDs concentrations should be closely related to the PLQYs of LSCs. Thus, the PLQYs of the B-LSC-SW and G-LSC-SW at 25 °C had been conducted by using integrating spheres and a fluorescence spectrophotometer. As shown in Supplementary Materials Figure S2, Tables S4 and S5, as for B-LSC-SWs, 24.08%, 31.59%, 34.84%, 27.51%, and 24.85% of PLQYs had been obtained with the gradual increase of B-CQDs concentrations. Moreover, the PLQYs of G-LSC-SWs were changed from 43.50%, 53.21%, 53.88%, and 42.67%, to 32.25% with the increased G-CQDs concentrations. Obviously, there is a maximum PLQY at an optimal condition (Supplementary Materials Figure S2), which is well matched with the changing trend of η_{opt} at the same CQDs concentrations. Thus, in this work, the PLQYs of LSCs played a key role in the performance of LSC-SW. On the other hand, the scattering effect also would affect the performances of LSC-SW. To further demonstrate the scattering effect, first, the control LSC-SW had been prepared, which only contain thermoresponsive polymer without CQDs. As shown in Supplementary Materials Figure S3, the η_{opt} was 0.88% at 25 °C and 2.84% at 35 °C, respectively. The results showed that the η_{opt} in the opaque state was ~3 times higher than that in the transparent state, thus, the increased efficiency only comes from the enhanced scattering effect in the opaque state since CQDs did not give any contribution. Second, the IPCE of LSC-SW was further measured to demonstrate the scattering effect, as shown in Supplementary Materials Figure S4. The results exhibited that the spectral response at opaque state showed a broadband response and was larger than that in the transparent state once above 500 nm of wavelength, further indicating the scattering effect also plays an important role in the performance of LSC-SW. Finally, the large-area LSC-SWs ($5 \times 5 \times 0.2 \text{ cm}^3$) were also prepared, as shown in Supplementary Materials Figure S5, the η_{opt} of B-LSC-SW was 2.37% at 25 °C and 5.22% at 35 °C, respectively. While the η_{opt} of G-LSC-SW was 2.44% at 25 °C and 5.31% at 35 °C, respectively. The results showed that all the η_{opt} of large-area LSC-SWs were lower than that of small-sized LSC-SWs (Figure 6), also resulting from the scattering effect. Therefore, the scattering effect would facilitate the performance enhancement of LSC-SWs at a small size.

3.3. Temperature Response of Laminated LSC-SWs

The temperature response of the B-LSC and G-LSC-SWs had further been demonstrated. Figure 7a,c show the transmittance of the optimal B- and G-LSC-SWs at different temperatures. It can be seen that the transmittance of both B-LSC-SWs and G-LSC-SWs appeared the same trend: the critical point of transmittance occurred at 32 °C (Supplementary Materials Figure S6), which well matched with the LCST transition of PNIPAm [43,52]. Based on this, the transmittance of B-LSC-SWs and G-LSC-SWs with different CQDs concentrations at varying ambient temperatures (25 °C and 35 °C) had been explored (Figure 7b,d). When the temperature was lower than 32 °C, all the LSC-SWs were transparent and had high transmittance (>70%), the transmittance of the optimal LSC-SWs could reach 83%. While all the LSC-SWs turned out to be opaque and showed low transmittance (<10%) once room temperature was higher than 32 °C. Thus, the LCST transition of PNIPAm played an important role in the tunability of the transparency of LSC-SWs.

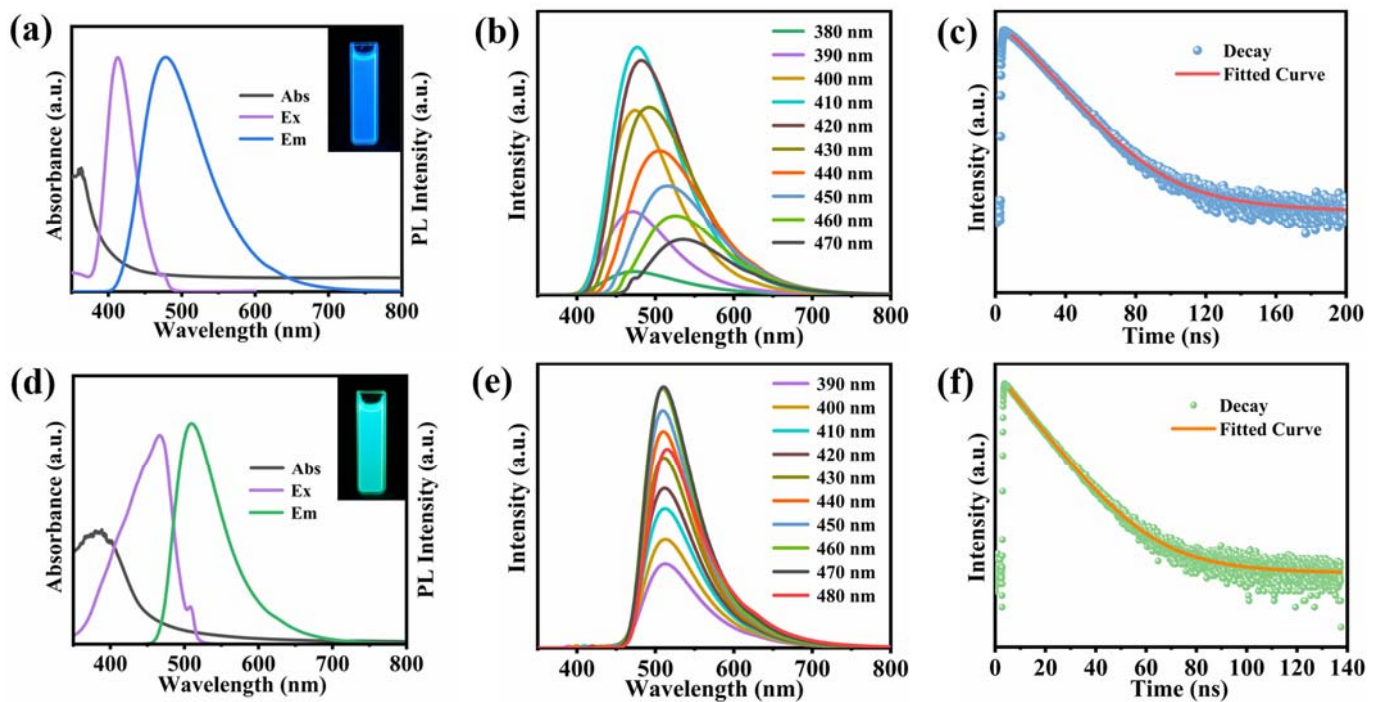


Figure 4. (a,d) The absorption, PL excitation and emission spectra of B-CQDs and G-CQDs, respectively (Insets are the corresponding photographs of B- and G-CQDs solution in cuvette under UV light). (b,e) PL spectra of B-CQDs and G-CQDs at various excitation wavelengths, respectively. (c,f) The PL decay spectra of B-CQDs and G-CQDs at 375 nm, respectively.

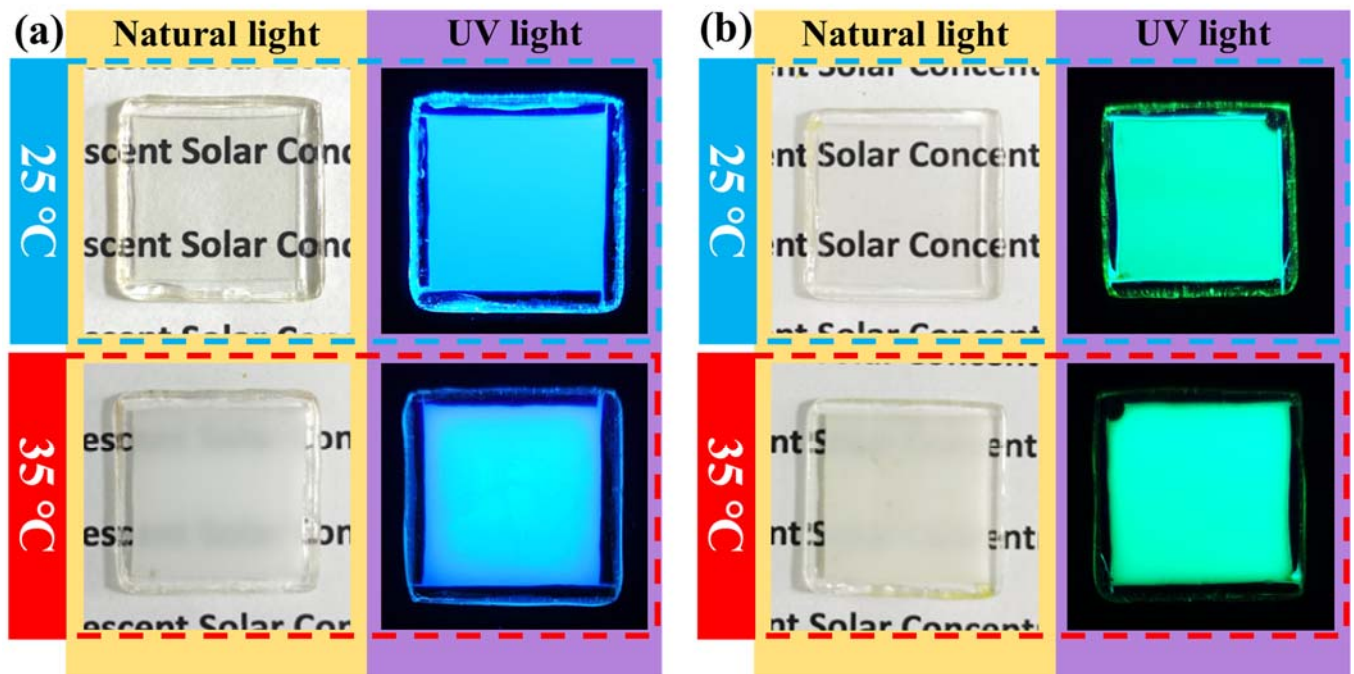


Figure 5. (a) Photograph of B-LSC-SW under natural light and 365 nm UV light at 25 °C and 35 °C, respectively. (b) Photograph of G-LSC-SW under natural light and 365 nm UV light at 25 °C and 35 °C.

Based on the good transparency tunability of B- or G-LSC-SWs with temperature, indoor temperature monitoring had been demonstrated, as shown in Figure 8. First, an indoor temperature monitoring device based on B-LSC-SW had been built, consisting of a hollow cubic box, B-LSC-SW ($10 \times 10 \times 0.3 \text{ cm}^3$) as a top wall window, and two temperature

sensors inside a box, as shown in Figure 8a. To avoid the effect of ambient temperature outside the box on the test data, all the box walls were wrapped with thermal insulation materials. For better comparison, a glass substrate, instead of LSC-SW, was also used as the top wall window of the box. Two temperature sensors were used to measure the indoor temperatures: sensor A measured the bottom temperature of the box and sensor B recorded the air temperature in the middle of the box, corresponding to the simulated indoor floor temperature and indoor air temperature. Figure 8b shows the temperature changes at different positions of the box with time. Under the irradiation of a standard sunlight intensity ($100 \text{ mW}/\text{cm}^2$), when the B-LSC-SW was used, the temperature slowly increased from 27.6°C to 29.4°C (the bottom temperature) and 28.9°C (the middle temperature) at the beginning of irradiation time (0–80 s), respectively. After that, both temperatures were almost kept constant. After 600 s of irradiation, the bottom temperature reached 30.6°C and the middle temperature was 29.6°C , respectively. By comparison, when the glass substrate was used to replace the LSC window, within 0–80 s, the temperature rapidly increased from 27.6°C to 39.4°C (the bottom temperature) and 31.0°C (the middle temperature), respectively. After 600 s of irradiation, the bottom temperature reached 42.8°C and the middle temperature is up to 32.6°C , respectively. The results showed that after 600 s irradiation, compared to that of the glass window, the LSC-SW could lead to 12.2°C of the bottom temperature difference and 3.0°C of the middle temperature difference, respectively. In addition, the whole indoor temperature could be controlled to be lower than 31°C after using LSC-SWs. Thus, the LSC-SWs posed great potential in indoor temperature modulation and energy saving.

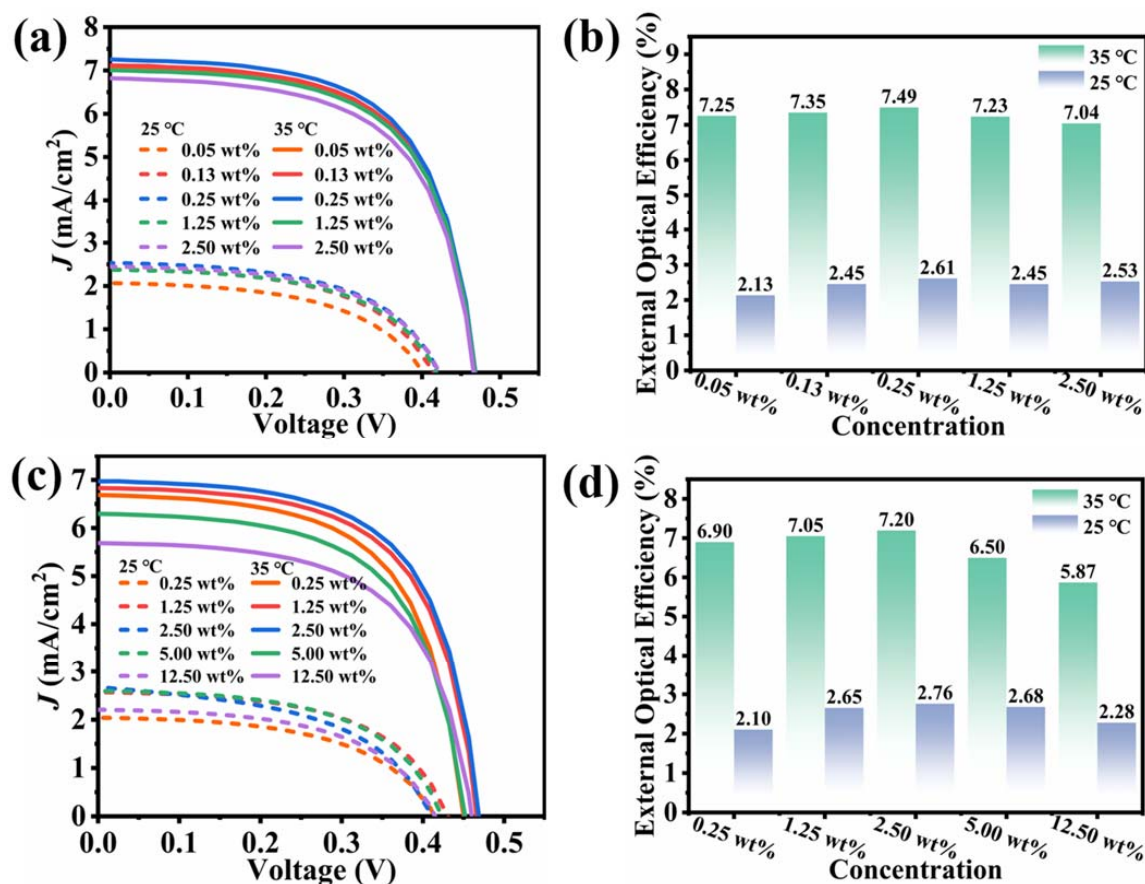


Figure 6. Relationship of the photocurrent density and photovoltage (J - V) of (a) B-LSC-SW and (c) G-LSC-SW with different CQDs concentration at 25°C and 35°C , respectively. The external optical efficiencies of (b) B-LSC-SWs and (d) G-LSC-SWs with different CQDs concentrations at 25°C and 35°C , respectively.

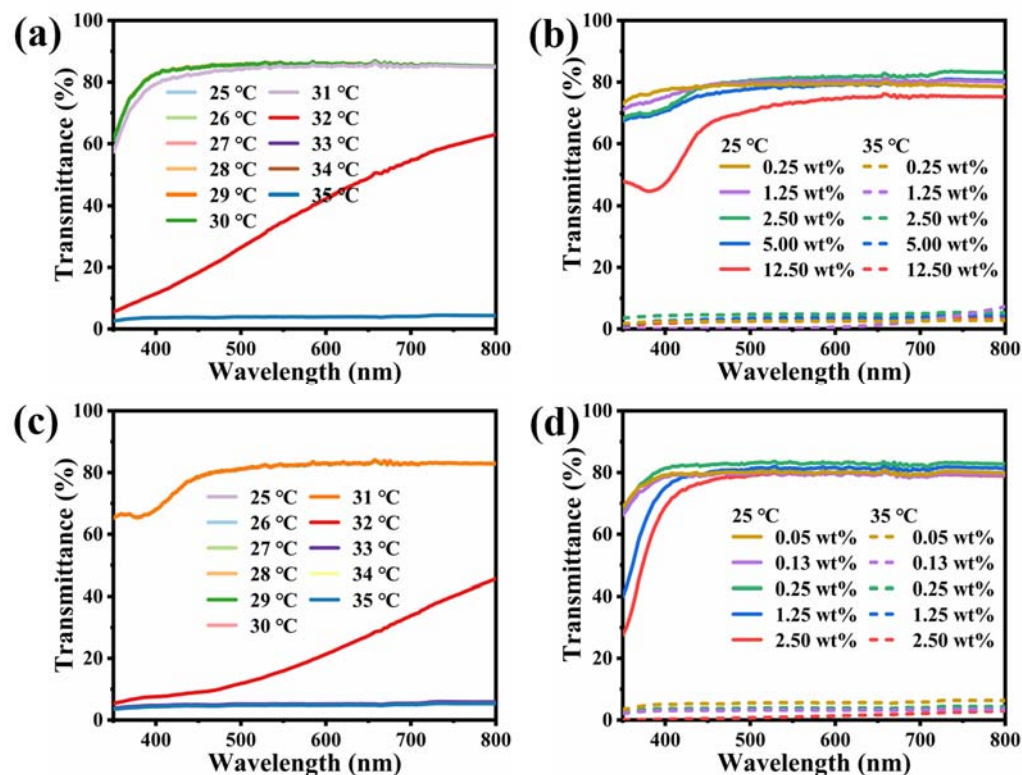


Figure 7. Transmittance spectra of (a) the optimal B-LSC-SW and (c) the optimal G-LSC-SW at different temperatures, respectively. Transmittance spectra of (b) B-LSC-SW and (d) G-LSC-SW with different CQDs concentrations at 25 °C and 35 °C, respectively.

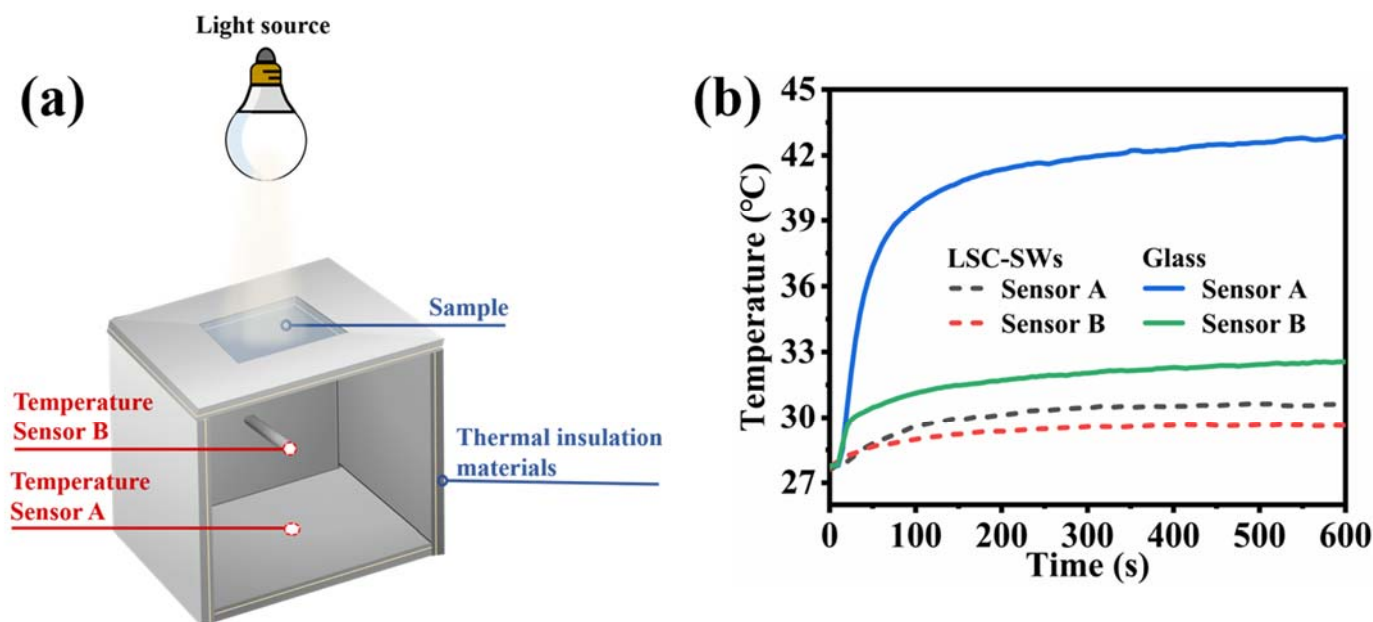


Figure 8. (a) Schematic diagram of indoor temperature monitoring device based on B-LSC-SW. (b) The temperature change at various indoor positions with the exposure time. Sensor A measured the temperature at the bottom of the device. Sensor B recorded the air temperature in the middle of the device. A standard sunlight (100 mW/cm²) was used to illuminate the window.

4. Conclusions

In summary, a novel thermoresponsive laminated LSC-SW was designed and prepared. The thermosensitive polymer and CQDs were chosen for the construction of the laminated

LSC-SWs. The LS-SWs are sensitive to the change in ambient temperature owing to the LCST transition of thermosensitive polymer. With the increased ambient temperature, the optimal LSC-SWs can change their transparency from a transparent state ($>80\%$ of transmittance, $<32\text{ }^{\circ}\text{C}$) to an opaque state ($<10\%$ of transmittance, $>32\text{ }^{\circ}\text{C}$). Furthermore, the LSC-SWs also had a good ability for electricity generation, the optimal η_{opt} of 7.49% in an opaque state can be achieved. Moreover, based on the optical tunability, the indoor temperature could be improved greatly, posing great potential in energy saving.

Supplementary Materials: The following supporting information can be downloaded at: <https://www.mdpi.com/article/10.3390/cryst12111612/s1>.

Author Contributions: Conceptualization, J.W.; methodology, J.W.; data curation, B.X.; investigation, J.W., B.X., C.C., W.X., L.W., Q.Y., B.P., Y.H. and J.L.; writing—original draft, J.W. and B.X.; writing—review and editing, J.W. and B.X.; funding acquisition, J.W. and J.L.; resources, J.W., L.W. and J.L.; supervision, J.W., L.W., J.L. and X.W. All authors have read and agreed to the published version of the manuscript.

Funding: This work was financially supported by the National Natural Science Foundation of China (Grant Nos. 51673060, 11574075), Science and Technology Department of Hubei province (Grant No. 2020BIB020), and the Ministry of Science and Technology of China (Grant No.2016YFA0200200). Overseas Expertise Introduction Center for Discipline Innovation (D18025) also gave part of support.

Institutional Review Board Statement: Not applicable.

Informed Consent Statement: Not applicable.

Data Availability Statement: Not applicable.

Conflicts of Interest: The authors declare no conflict of interest.

References

1. Vasiliev, M.; Nur-E-Alam, M.; Alameh, K. Recent developments in solar energy-harvesting technologies for building integration and distributed energy generation. *Energies* **2019**, *12*, 1080. [\[CrossRef\]](#)
2. Nie, Y.; He, W.; Liu, X.; Hu, Z.; Yu, H.; Liu, H. Smart luminescent solar concentrator as a BICPV window. *Build. Simul.* **2022**, *15*, 1789–1798. [\[CrossRef\]](#)
3. Debije, M.G.; Verbunt, P.P.C. Thirty years of luminescent solar concentrator research: Solar energy for the built environment. *Adv. Energy Mater.* **2012**, *2*, 12–35. [\[CrossRef\]](#)
4. Papakonstantinou, I.; Portnoi, M.; Debije, M.G. The hidden potential of luminescent solar concentrators. *Adv. Energy Mater.* **2020**, *11*, 2002883. [\[CrossRef\]](#)
5. Iasilli, G.; Francischello, R.; Lova, P.; Silvano, S.; Surace, A.; Pesce, G.; Allosio, M.; Patrini, M.; Shimizu, M.; Comoretto, D.; et al. Luminescent solar concentrators: Boosted optical efficiency by polymer dielectric mirrors. *Mater. Chem. Front.* **2019**, *3*, 429–436. [\[CrossRef\]](#)
6. Li, Z.; Zhao, X.; Huang, C.; Gong, X. Recent advances in green fabrication of luminescent solar concentrators using nontoxic quantum dots as fluorophores. *J. Mater. Chem. C* **2019**, *7*, 12373–12387. [\[CrossRef\]](#)
7. Kim, A.; Hosseinmardi, A.; Annamalai, P.K.; Kumar, P.; Patel, R. Review on colloidal quantum dots luminescent solar concentrators. *ChemistrySelect* **2021**, *6*, 4948–4967. [\[CrossRef\]](#)
8. Papucci, C.; Charaf, R.; Coppola, C.; Sinicropi, A.; di Donato, M.; Taddei, M.; Foggi, P.; Battisti, A.; de Jong, B.; Zani, L.; et al. Luminescent solar concentrators with outstanding optical properties by employment of D-A-D quinoxaline fluorophores. *J. Mater. Chem. C* **2021**, *9*, 15608–15621. [\[CrossRef\]](#)
9. Zhao, H.; Zhou, Y.; Benetti, D.; Ma, D.; Rosei, F. Perovskite quantum dots integrated in large-area luminescent solar concentrators. *Nano Energy* **2017**, *37*, 214–223. [\[CrossRef\]](#)
10. Li, Y.; Miao, P.; Zhou, W.; Gong, X.; Zhao, X. N-doped carbon-dots for luminescent solar concentrators. *J. Mater. Chem. A* **2017**, *5*, 21452–21459. [\[CrossRef\]](#)
11. Zhou, Y.; Zhao, H.; Ma, D.; Rosei, F. Harnessing the properties of colloidal quantum dots in luminescent solar concentrators. *Chem. Soc. Rev.* **2018**, *47*, 5866–5890. [\[CrossRef\]](#)
12. Ma, W.; Li, W.; Liu, R.; Cao, M.; Zhao, X.; Gong, X. Carbon dots and AIE molecules for highly efficient tandem luminescent solar concentrators. *Chem. Commun.* **2019**, *55*, 7486–7489. [\[CrossRef\]](#)
13. Mateen, F.; Ali, M.; Lee, S.Y.; Jeong, S.H.; Ko, M.J.; Hong, S.-K. Tandem structured luminescent solar concentrator based on inorganic carbon quantum dots and organic dyes. *Solar Energy* **2019**, *190*, 488–494. [\[CrossRef\]](#)
14. Cohen, T.A.; Milstein, T.J.; Kroupa, D.M.; MacKenzie, J.D.; Luscombe, C.K.; Gamelin, D.R. Quantum-cutting Yb³⁺-doped perovskite nanocrystals for monolithic bilayer luminescent solar concentrators. *J. Mater. Chem. A* **2019**, *7*, 9279–9288. [\[CrossRef\]](#)

15. Roncali, J. Luminescent solar collectors: Quo Vadis? *Adv. Energy Mater.* **2020**, *10*, 2001907. [[CrossRef](#)]
16. Zdražil, L.; Kalytchuk, S.; Holá, K.; Petr, M.; Zmeškal, O.; Kment, S.; Rogach, A.L.; Zbořil, R. A carbon dot-based tandem luminescent solar concentrator. *Nanoscale* **2020**, *12*, 6664–6672. [[CrossRef](#)] [[PubMed](#)]
17. Wang, J.; Wang, J.; Xu, Y.; Jin, J.; Xiao, W.; Tan, D.; Li, J.; Mei, T.; Xue, L.; Wang, X. Controlled synthesis of long-wavelength multicolor-emitting carbon dots for highly efficient tandem luminescent solar concentrators. *ACS Appl. Mater. Interfaces* **2020**, *3*, 12230–12237. [[CrossRef](#)]
18. Zhao, H.; Liu, G.; You, S.; Camargo, F.V.A.; Zavelani-Rossi, M.; Wang, X.; Sun, C.; Liu, B.; Zhang, Y.; Han, G.; et al. Gram-scale synthesis of carbon quantum dots with a large Stokes shift for the fabrication of eco-friendly and high-efficiency luminescent solar concentrators. *Energy Environ. Sci.* **2021**, *14*, 396–406. [[CrossRef](#)]
19. Wu, J.; Xin, W.; Wu, Y.; Zhan, Y.; Li, J.; Wang, J.; Huang, S.; Wang, X. Solid-state photoluminescent silicone-carbon dots/dendrimer composites for highly efficient luminescent solar concentrators. *Chem. Eng. J.* **2021**, *422*, 130158. [[CrossRef](#)]
20. Han, Y.; Zhao, X.; Vomiero, A.; Gong, X.; Zhao, H. Red and green-emitting biocompatible carbon quantum dots for efficient tandem luminescent solar concentrators. *J. Mater. Chem. C* **2021**, *9*, 12255–12262. [[CrossRef](#)]
21. Li, J.; Zhao, H.; Zhao, X.; Gong, X. Red and yellow emissive carbon dots integrated tandem luminescent solar concentrators with significantly improved efficiency. *Nanoscale* **2021**, *13*, 9561–9569. [[CrossRef](#)] [[PubMed](#)]
22. Han, Y.; Liccardo, L.; Moretti, E.; Zhao, H.; Vomiero, A. Synthesis, optical properties and applications of red/near-infrared carbon dots. *J. Mater. Chem. C* **2022**, *10*, 11827–11847. [[CrossRef](#)]
23. Xin, W.; Wang, J.; Xu, B.; Wu, J.; Wang, J.; Ren, Z.; Cai, C.; Xue, C.; Li, J.; Wang, X. Construction of highly efficient carbon dots-based polymer photonic luminescent solar concentrators with sandwich structure. *Nanotechnology* **2022**, *33*, 305601. [[CrossRef](#)] [[PubMed](#)]
24. Kim, H.N.; Yang, S. Responsive smart windows from nanoparticle–polymer composites. *Adv. Funct. Mater.* **2019**, *30*, 1902597. [[CrossRef](#)]
25. Zhang, W.; Wang, C.; Chen, K.; Yin, Y. Raspberry-shaped thermochromic energy Storage nanocapsule with tunable sunlight absorption based on color change for temperature regulation. *Small* **2019**, *15*, e1903750. [[CrossRef](#)] [[PubMed](#)]
26. Zhuang, B.; Dai, Z.; Pang, S.; Xu, H.; Sun, L.; Ma, F. 3D ordered macroporous VO₂ thin films with an efficient thermochromic modulation capability for advanced smart windows. *Adv. Opt. Mater.* **2019**, *7*, 1900600. [[CrossRef](#)]
27. Xie, Y.; Guan, F.; Li, Z.; Meng, Y.; Cheng, J.; Li, L.; Pei, Q. A phase-changing polymer film for broadband smart window applications. *Macromol. Rapid Commun.* **2020**, *41*, e2000290. [[CrossRef](#)]
28. Li, K.; Meng, S.; Xia, S.; Ren, X.; Gao, G. Durable and controllable smart windows based on thermochromic hydrogels. *ACS Appl. Mater. Interfaces* **2020**, *12*, 42193–42201. [[CrossRef](#)] [[PubMed](#)]
29. Zhou, Y.; Dong, X.; Mi, Y.; Fan, F.; Xu, Q.; Zhao, H.; Wang, S.; Long, Y. Hydrogel smart windows. *J. Mater. Chem. A* **2020**, *8*, 10007–10025. [[CrossRef](#)]
30. Torres-Pierna, H.; Ruiz-Molina, D.; Roscini, C. Highly transparent photochromic films with a tunable and fast solution-like response. *Mater. Horiz.* **2020**, *7*, 2749–2759. [[CrossRef](#)]
31. Chen, G.; Hong, W. Mechanochromism of structural-colored materials. *Adv. Opt. Mater.* **2020**, *8*, 2000984. [[CrossRef](#)]
32. Hu, F.; Yan, B.; Ren, E.; Gu, Y.; Lin, S.; Ye, L.; Chen, S.; Zeng, H. Constructing spraying-processed complementary smart windows via electrochromic materials with hierarchical nanostructures. *J. Mater. Chem. C* **2019**, *7*, 14855–14860. [[CrossRef](#)]
33. Islam, S.M.; Palma, A.A.; Gautam, R.P.; Barile, C.J. Hybrid dynamic windows with color neutrality and fast switching using reversible metal electrodeposition and cobalt hexacyanoferrate electrochromism. *ACS Appl. Mater. Interfaces* **2020**, *12*, 44874–44882. [[CrossRef](#)]
34. Zheng, R.; Wang, Y.; Pan, J.; Malik, H.A.; Zhang, H.; Jia, C.; Weng, X.; Xie, J.; Deng, L. Toward easy-to-assemble, large-area smart windows: All-in-one cross-linked electrochromic material and device. *ACS Appl. Mater. Interfaces* **2020**, *12*, 27526–27536. [[CrossRef](#)] [[PubMed](#)]
35. Feng, M.; Bu, X.; Yang, J.; Li, D.; Zhang, Z.; Dai, Y.; Zhang, X. Review: Smart windows based on photonic crystals. *J. Mater. Sci.* **2020**, *55*, 8444–8463. [[CrossRef](#)]
36. Zhang, S.; Cao, S.; Zhang, T.; Lee, J.Y. Plasmonic oxygen-deficient TiO₂-x nanocrystals for dual-band electrochromic smart windows with efficient energy recycling. *Adv. Mater.* **2020**, *32*, e2004686. [[CrossRef](#)]
37. Wang, J.L.; Sheng, S.Z.; He, Z.; Wang, R.; Pan, Z.; Zhao, H.Y.; Liu, J.W.; Yu, S.H. Self-powered flexible electrochromic smart window. *Nano. Lett.* **2021**, *21*, 9976–9982. [[CrossRef](#)]
38. Wang, Z.; Jia, X.; Zhang, P.; Liu, Y.; Qi, H.; Zhang, P.; Kaiser, U.; Reineke, S.; Dong, R.; Feng, X. Viologen-immobilized 2D polymer film enabling highly efficient electrochromic device for solar-powered smart window. *Adv. Mater.* **2022**, *34*, e2106073. [[CrossRef](#)]
39. Sol, J.; Dehm, V.; Hecht, R.; Würthner, F.; Schenning, A.; Debije, M.G. Temperature-responsive luminescent solar concentrators: Tuning energy transfer in a liquid crystalline matrix. *Angew. Chem. Int. Ed.* **2018**, *57*, 1030–1033. [[CrossRef](#)]
40. Sol, J.A.H.P.; Timmermans, G.H.; Breugel, A.J.; Schenning, A.P.H.J.; Debije, M.G. Multistate luminescent solar concentrator “smart” windows. *Adv. Energy Mater.* **2018**, *8*, 1702922. [[CrossRef](#)]
41. Mateen, F.; Ali, M.; Oh, H.; Hong, S.-K. Nitrogen-doped carbon quantum dot based luminescent solar concentrator coupled with polymer dispersed liquid crystal device for smart management of solar spectrum. *Sol. Energy* **2019**, *178*, 48–55. [[CrossRef](#)]
42. Havrlík, M.; Libra, M.; Poulek, V.; Kouřim, P. Analysis of Output Signal Distortion of Galvanic Isolation Circuits for Monitoring the Mains Voltage Waveform. *Sensors* **2022**, *22*, 7769. [[CrossRef](#)]

43. Li, X.-H.; Liu, C.; Feng, S.-P.; Fang, N.X. Broadband light management with thermochromic hydrogel microparticles for smart windows. *Joule* **2019**, *3*, 290–302. [[CrossRef](#)]
44. Zhang, Y.; Song, H.; Wang, L.; Yu, J.; Wang, B.; Hu, Y.; Zang, S.Q.; Yang, B.; Lu, S. Solid-state red laser with a single longitudinal mode from carbon dots. *Angew. Chem. Int. Ed.* **2021**, *60*, 25514–25521. [[CrossRef](#)] [[PubMed](#)]
45. Yang, C.; Atwater, H.A.; Baldo, M.A.; Baran, D.; Barile, C.J.; Barr, M.C.; Bates, M.; Bawendi, M.G.; Bergren, M.R.; Borhan, B.; et al. Consensus statement: Standardized reporting of power-producing luminescent solar concentrator performance. *Joule* **2022**, *6*, 8–15. [[CrossRef](#)]
46. Rana, M.M.; Rajeev, A.; Natale, G.; De la Hoz Siegler, H. Effects of synthesis-solvent polarity on the physicochemical and rheological properties of poly(N-isopropylacrylamide) (PNIPAm) hydrogels. *J. Mater. Res. Technol.* **2021**, *13*, 769–786. [[CrossRef](#)]
47. Jadhav, S.A.; Brunella, V.; Miletto, I.; Berlier, G.; Scalarone, D. Synthesis of poly(N-isopropylacrylamide) by distillation precipitation polymerization and quantitative grafting on mesoporous silica. *J. Appl. Polym. Sci.* **2016**, *133*, 44181. [[CrossRef](#)]
48. Li, F.; Li, Y.; Yang, X.; Han, X.; Jiao, Y.; Wei, T.; Yang, D.; Xu, H.; Nie, G. Highly fluorescent chiral N-S-doped carbon dots from cysteine: Affecting cellular energy metabolism. *Angew. Chem. Int. Ed.* **2018**, *57*, 2377–2382. [[CrossRef](#)] [[PubMed](#)]
49. Zhang, Y.; Liu, X.; Fan, Y.; Guo, X.; Zhou, L.; Lv, Y.; Lin, J. One-step microwave synthesis of N-doped hydroxyl-functionalized carbon dots with ultra-high fluorescence quantum yields. *Nanoscale* **2016**, *8*, 15281–15287. [[CrossRef](#)]
50. Talite, M.J.; Huang, H.Y.; Wu, Y.H.; Sena, P.G.; Cai, K.B.; Lin, T.N.; Shen, J.L.; Chou, W.C.; Yuan, C.T. Greener luminescent solar concentrators with high loading contents based on in situ cross-linked carbon nanodots for enhancing solar energy harvesting and resisting concentration-induced quenching. *ACS Appl. Mater. Interfaces* **2018**, *10*, 34184–34192. [[CrossRef](#)]
51. Zhang, Y.; Li, C.; Fan, Y.; Wang, C.; Yang, R.; Liu, X.; Zhou, L. A self-quenching-resistant carbon nanodot powder with multicolored solid-state fluorescence for ultra-fast staining of various representative bacterial species within one minute. *Nanoscale* **2016**, *8*, 19744–19753. [[CrossRef](#)] [[PubMed](#)]
52. Zhou, Y.; Wang, S.; Peng, J.; Tan, Y.; Li, C.; Boey, F.Y.C.; Long, Y. Liquid thermo-responsive smart window derived from hydrogel. *Joule* **2020**, *4*, 2458–2474. [[CrossRef](#)]